Chapter IV

Mechanism of Wurtzite $CuInS_2$ NPs Formation

IV.1 Introduction

The solution-based methods of producing $CuIn_xGa_{1-x}(S, Se)_2$ (CIGS) absorbers layer can be described as a two-step process; initial synthesis of CIGS ink (Molecular and nanoparticle routes) followed by deposition. Establishing the wz-CIS nanoparticle synthesis and ink formation would be the first step for utilizing transformation-assisted grain growth to achieve a large grained ch-CIS absorber layer. There are several reports on solution synthesis of phase pure wz-CIS NPs following different approaches [44, 46, 47, 175–178], utilising different precursor salts such as metal-nitrates, acetylacetonates, acetates, chlorides and iodides dissolved into a varieties of solvent such as ethylene glycol, hexadecylamine, oleylamine, diethylene glycol, oleic acid, ethylenediamine, trioctylphosphine oxide, 1-dodecanethiol, tert-dodecanethiol [179]. Among the solvent combinations, amine and thiol received much attention because of the ease in controlling the solubility of chalcogenides and dissolution of a variety of metal salts such as metal chloride [95], metal acetylacetonates [172], metal iodide [180], and metal nitrides [181]. In addition to that residue impurities (C, N, O, etc.) induced by capping agent amine and stabilizing agent thiol are easily removed from the final product by washing [95, 177, 182–186].

Fast reaction rates and the presence of thiols in the reaction solution favours the stabilization of wurtzite phase [184]. However, there are several factors such as temperature, concentration and nature of precursors and solvents that allows for the fine-tuning of the composition, size and shape of the resulting nanocrystals. There are contradictory reports on the effect of temperature; one reports suggests wz-CIS is favoured at lower temperature [47, 180, 187, 188], while the other suggest the contrary [177, 189]. Similarly, the role of thiols and formation of Cu-S phases are still not clear [44, 190]. Some reports suggest that the amine group (hard acid) binds with the indium precursor (hard base) and reduces the precipitation rate of In_2S_3 providing for initial precipitation of Cu_2S which acts as seed for formation of wz-CIS [184, 190, 191]. However, the exact reaction pathways for the wz-CIS formation during amino-thiol hot-injection synthesis is not well stablished. For the synthesis of phase pure wz-CIS, and utilize it for the formation of large grained ch-CIS films, it is important to get insight into the formation mechanism and the control parameters.

In this chapter, the formation mechanism of wz-CIS is discussed. Cu–In–S nanoparticles were solution-processed using metal acetylacetonate precursors, OAm and TOPO as active ligands. The role of active ligand (OAm and TOPO) in phase evolution as a function of temperature has been studied utilizing Fourier-transform infrared spectroscopy (FTIR) and X-ray diffraction (XRD) analysis, while the nanoparticle morphology, crystallography and elemental distribution has been characterized by transmission electron microscopy (TEM).

IV.2 A Review of Relevant Literature

The effect of processing parameters such as time, temperature, ligands, and precursor on the size, morphology, and crystallography of the metastable wz-CIS phase have been extensively reported [95, 172, 177, 181–184, 192]. In 2008, Pan *et. al.* [44] used copper and indium diethyl-dithiocarbamate in octadecene, with oleylamine as surfactant and 1-dodecanethiol as ligands, to obtain wurtzite structures. They claimed that the wz-CIS nanocrystals were obtained by using dodecanethiol as the capping agent instead of oleic acid, which lead the formation zincblende structure. Norako *et al.* [193] specified the preferred molar ratios of oleylamine and 1-dodecanethiol as 14:0 and 12:2, for the formation of wurtzite phase. On the other hand, Qi *et al.* [47] suggested that the coordination between Cu^{2+} and ligand such as ethanolamine molecules ($-NH_2$) favour the nucleation and growth of wz-CIS through during solvothermal processing. Koo *et al.* [194] used a thiourea instate of thiols as sulfur source to form wz-CIS nanocrystals in the presence of an OAm. They have reported the formation wurtzite-chalcopyrite polytypism with coexistence of both wurtzite and chalcopyrite domains interface across (002)/(112) stacking. Nose *et al.* [178] showed that wurtzite phase appears during synthesis when the metallic monomers (CuI and $InCl_3$) were coordinated with hexadecylamine or oleylamine. Batabyal *et al.* [177] shows that the influence of temperature on the phase formation utilizing a single source precursor ($(Ph_3P)CuIn(SC\{O\}Ph)_4$) in the presence of 1-DDT or TOOP. Pure wz-CIS phase was obtained at lower temperatures (150-250^oC) with high TOOP concentration, and single zincblende CIS phase were obtained, when the synthesis was conducted at 350 °C. Chang *et al.* [180] also reported the low temperature synthesis of wz-CIS

particles in presence of coordinating solvent (OAm). On the contrary, Kruszynska *et al.* [184] reported the formation of wurtzite structure at higher temperatures in presence of thiols, while at lower temperature zincblende structure appeared.

There were several reports, which shows that the formation of wz-CIS phase begins with Cu–S phase nucleation [44, 181, 190, 191, 195, 196], which can also be supported by having nearly the same anion lattice of hexagonal Cu_2S and CIS, albeit without extending any direct evidence in most cases. Copper deficient phases formed by the copper sulfide, which exhibit high cation mobility at low temperatures. This eases the exchange with In^{3+} ions that have the same radius as Cu^{+}. Moreover, wurtzite CIS and copper sulfide share the same anionic sublattice. Hence, phase transformation from copper sulfide to CIS requires little lattice distortion and is encouraged by the high cation mobility. The basic challenge that arises for the formation of wz-CIS NPs is the fact that two cations of this ternary I-III-VI_2 semiconductor have different chemical properties. In^{3+} is a hard Lewis acid, while Cu^{+} is a soft acid. Therefore, these cations have different reactivity towards sulfur compounds.

Connor *et al.* [195] and Kruszynska *et al.* [196] were the first to extend the direct evidence of the formation of Cu–S using high resolution TEM as the initial phase during the solution processing of wz-CIS. Connor *et al.* [195] synthesized the wz-CIS nanorods, which began with the formation of copper sulfide nanodiscs and then CIS NPs grew on one side (Biphasic structure ,Cu_2S and CISu phases). Finally, after 20 min reaction, biphasic structure converted completely into wz-CIS NPs. Kruszynska *et al.* [196] showed that copper sulfide particles could act as seeds for wz-CIS which during the course of reaction, had given way to a two phase hybrid

NPs, eventually forming single phase wz-CIS nanocrystals. Li *et al.* [192] and Tang *et al.* [190] reported the formation of monoclinic $Cu_{1.75}S$ and $Cu_{1.94}S$ nanocrystal before the growth of wz-CIS NPs. However, both groups did not discuss the reason behind the formation of Cu–S. It has been demonstrated that the active ligand (oleylamine, 1-dodecanethiol, etc.) species play a critical role in the synthesis of wz-CIS NPs [177, 178, 191, 193]. Coughlan *et al.* [182] reported the presence of mixed phases of copper sulfide, both hexagonal (chalcocite Cu_2S, covellite CuS) and orthorhombic (anilite Cu_7S_4), which subsequently yielded the quaternary CIGS phase. Although, it is more or less accepted that Cu–S forms during the initial stages of solution synthesis, however, there is still some ambiguity about the exact oxidation state of Cu (i.e. Cu_2S, CuS and Cu_7S_4). On the contrary, Norako *et al.* [193] and Qi *et al.* [47] did not observe any Cu–S formation during solution processing of wz-CIS particles. Zhang *et al.* [197] discussed the formation of CIGS NPs based on Cu–S nucleation, although did not comment much about the growth process. Apart from Copper sulfide, Ag_2S has also been demonstrated to act as a seed for CIS NPs. Li *et al.* [198] demonstrated the formation of wz-CIS nanowires using Ag_2S as seed. Interestingly, the lattice mismatch between Ag_2S and CIS is nearly same as that of $Cu_{1.75}S$ and CIS [192]. However, to the best of our knowledge, a detailed and systematic study of the phase progression and role of trioctylphosphine oxide (TOPO) and oleylamine (OAm) during wz-CIS solution processing utilizing metal acetylacetone precursors has not been discussed with evidence.

IV.3 Experimental Procedure

Wurtzite (wz) CIS NPs were synthesized by a solution-based processing route. For synthesizing wz-CIS NPs, 0.261 g (1 mmol) of $Cu(acac)_2$, 0.412 g (1 mmol) of $In(acac)_3$ and 1.353 g of TOPO were mixed with 10 ml of OAm in 100 ml three-neck round-bottom flask (RBF) at room temperature (RT). The solution was stirred at 100 rpm at RT for 30 min and was purged with ultra-pure nitrogen gas in a rota-mantle (LabQuest, Borosil, India) to remove any trapped air. After 30 min, the temperature of the solution was raised. The color of the solution became sky blue and turned slightly transparent at 50 °C. On increasing the temperature to 100 °C, the solution became light green and at 150 °C, it turned dark green. When the temperature of the reaction mixture reached 160 °C, a mixture of 0.25 ml of 1-DDT and 1.75 ml of t-DDT was rapidly injected through a syringe (2 ml) into the solution while the solution was continuously stirred. The solution turned essentially transparent with a light-yellow tint without any sign of precipitation. After injecting thiols, the temperature was further raised to 310 °C and was held at that temperature for ~60 min till the color of the solution became black. Meanwhile, samples were collected from the reaction mixture at intermediate temperatures (160, 200, 250, and 290 °C) with the help of a syringe. After 60 min of hold at 310 °C, the rota-mantle was switched off and the sample was allowed to cool down to RT, while being continuously purged with nitrogen. All reactions were performed in a schlenk line setup kept inside a fume hood. The NPs were separated from the solution by washing with ethanol and hexane followed by centrifuging (Remi group, India) at ~10,000 rpm for 8 min. The washing steps were performed to ensure the removal of capped ligand and un-reacted byproducts. After washing three times, most of the

residues were removed, and the as-synthesized wz-CIS NPs could be seen dispersed in a transparent liquid (Toluene).

IV.4 Results

To get insight into the formation mechanism of wz-CIS, samples were collected at intermediate stages of processing at 160, 200, 250 and 290 ℃, while the final sample was collected after keeping at 310 ℃ for 60 min.

IV.4.1 XRD Analysis

Room temperature XRD patterns obtained from the samples extracted at temperatures 160 ℃ and 200 ℃, had faint peaks at 2θ values 26.49°, 29.96°, 38.79°, 46.55° and 50.61°, which could be indexed to a crystallographic plane $(10\bar{1}0)$, $(10\bar{1}1)$, $(10\bar{1}2)$, $(11\bar{2}0)$ and $(10\bar{1}3)$ respectively of a hexagonal Cu_2S phase. The lattice constants of the Cu_2S phase, a = 3.89 Å and c = 6.41 Å were calculated from the XRD pattern, which was close to the reported lattice parameters of Cu_2S [180,199]. This observation was in accordance to the mechanism proposed by Kuzuya *et al.* [191], where the formation of a Cu–S compound (without showing direct evidence) in the presence of the active ligand (OAm) was suggested, which at the later stages was observed to convert into wz-CIS through an ion exchange reaction. The crystallite size of hexagonal Cu_2S was estimated from the peak broadening utilizing the Sherrer equation: , where λ is Cu-Kα wavelength, β is the full width at the half maximum (FWHM) of the XRD peak, θ is the Bragg's angle. The estimated crystallite size for the samples, extracted at 160 and 200 ℃, were 18 and 27 nm, respectively. On increasing temperature further to 250 ℃, the existing

diffraction peaks were shifted slightly to lower 2θ values (**Figure IV.1**, marked by red color dotted line), at the same time, new diffraction peaks, which were barely visible earlier, became prominent. XRD peaks located at 2θ values 26.36°, 27.75°, 29.80°, 38.62°, 46.40°, 50.37°, 54.16°, 54.97°, 56.18°, 57.33°, 61.95° and 64.15° were assigned to the crystallographic planes $(10\bar{1}0)$, (0002), $(10\bar{1}1)$, $(10\bar{1}2)$, $(11\bar{2}0)$, $(10\bar{1}3)$, $(11\bar{2}2)$, $(20\bar{2}0)$, $(20\bar{2}1)$, (0004), $(20\bar{2}2)$ and $(10\bar{1}4)$ of a wz-CIS phase, respectively. The lattice constants of wz-CIS, $a = 3.91 \pm 0.01$ Å and $c = 6.43 \pm 0.01$ Å, calculated from the NPs diffraction pattern were in good agreement with the values reported for CIS earlier by others [44, 184]. The XRD pattern showed a systematic peak shift toward lower angles on increasing temperature. This systematic peak shift was indicative of the increased size of the unit cell due to the ion exchange reaction, where In^{3+} ions were able to dissociate from thiol complexes and diffuse into the already nucleated Cu_2S resulting in the formation of wz-CIS. The expansion of the unit cell is easily fathomable as the In^{3+} (0.80 Å) ions are slightly larger in size when compared to Cu^{+} (0.77 Å). Peak shifting was in good agreement with simulated patterns (bottom of **Figure IV.1**), lattice parameters are quite comparable with experimental data **(Table IV.1)**. No XRD peak corresponding to In_2S_3 phase could be detected from the XRD, indicating that In_2S_3, if at all present, was lesser than the detection limit of XRD. From the XRD pattern, significant peak broadening was observed at 160 °C and this broadening of peaks was attributed to the smaller crystallite size. The XRD peak broadening decreased with an increase in growth temperature, which was a clear indication of larger crystallite sizes. However, on further processing above 250 °C, the peak width (β) remained almost constant, indicating that the crystallite size did not change substantially beyond the 250 °C. It may be due to the depletion of reactant or

consumption of ions from a solution that caused the size to reach the saturation limit by 250 °C, and therefore, no further growth from the solution was possible.

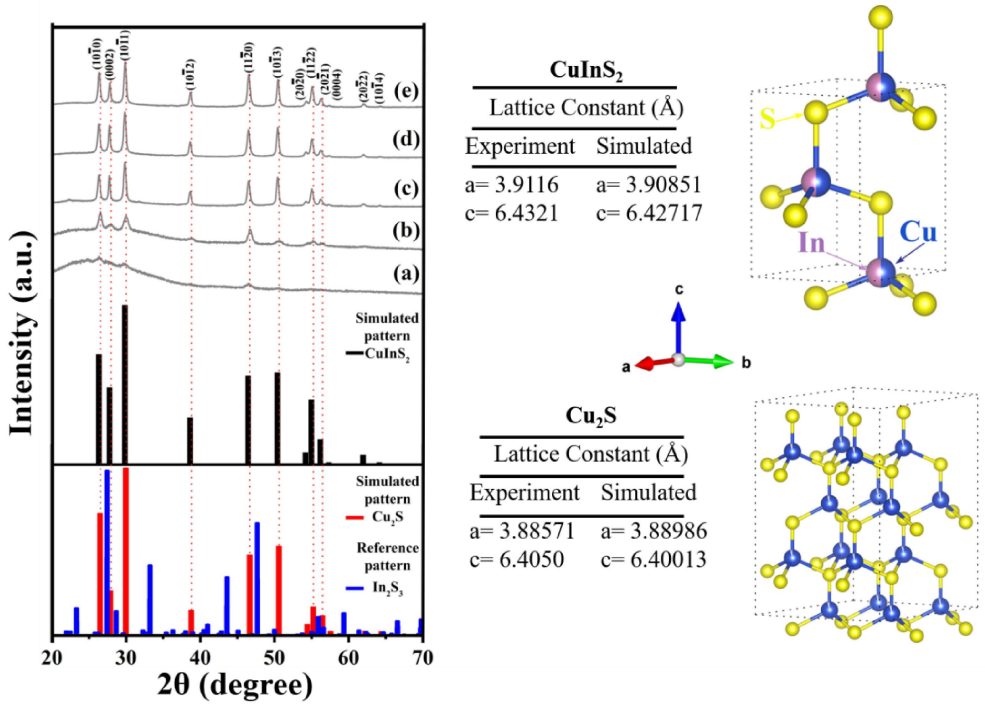

Figure IV.1 X-ray diffraction patterns, demonstrating the progressive evolution of peaks of $CuInS_2$ nanoparticles as taken from the reaction mixture at temperatures (a) 160 °C, (b) 200 °C, (c) 250 °C, (d) 290 °C, (e) 310 °C. (The red, blue and black solid line a at the bottom of (a) are the simulated diffraction patterns of the wurtzite phase of Cu_2S, In_2S_3 and CIS respectively. Crystal structure of wz-CIS (right top corner) and Cu_2S (right bottom corner), where Cu and In atoms occupy the same position, and each occupation is 50% in case wz-CIS).

Table IV.1 Crystal data and structural parameter of simulated ($CuInS_2$ and Cu_2S) and reference (In_2S_3) the diffraction patterns.

Crystal data											
Formula	$CuInS_2$			Cu_2S		In_2S_3 (COD: 4000813)					
Crystal structure	Hexagonal			Hexagonal		Tetragonal					
Space group	P63mc (186)			P63mc (186)		I 41/amd (141)					
Unit cell dimensions	a = b =3.91Å c =6.43Å			a=b=3.89Å c=6.40 Å		a=b=7.62 Å c=32.36 Å					
Structure parameters											
Atom	Cu	In	S	Cu	S	In	In	In	S	S	S
Wyck.	2b	2b	2b	2b	2b	8c	16h	8e	16h	16h	16h
x	0.333	0.333	0.333	0.333	0.333	0.000	0.000	0.000	0.000	0.000	0.000
y	0.666	0.666	0.666	0.666	0.666	0.000	-0.01	0.250	0.506	0.009	0.022
z	0.000	0.000	0.375	0.021	0.354	0.000	0.332	0.204	0.250	0.078	0.413
Occ.	0.5	0.5	1	0.951	0.991	1	1	1	1	1	1

IV.4.2 FTIR Analysis

In order to get insight into the intermediate compounds and the presence of functional groups on the surface of NPs during the processing of wz-CIS, the FTIR of the samples, extracted at different stages, were recorded. The processing was divided into two parts: (I) Metal precursor with the active ligand (OAm and TOPO) before the addition of thiols (≤150 °C) **(Figure IV.2)**, and (II) After the addition of thiols (1-DDT and t-DDT, ≥150 °C) (**Figure IV.4**) in a reaction mixture that included Cu(acac), In(acac), OAm and TOPO. Initially, the FTIR spectra of OAm and TOPO were separately recorded **(Figure IV.2(a) and (b))** while the list of absorption bands is tabulated in **Table IV.2**. The pure OAm had absorption bands at 3297, 3003, 2920, 2851, 1645,1611, 1584, 1463, 1070, 966, 794 and 721 cm^{-1}, which could be assigned to $\nu s(NH_2)$, $\delta(=C–H)$, $\nu s(C–H)$, $\nu as(C–H)$, $\delta(-C=C)$, combine the motion of NH_2 scissoring and N–H bending, $\delta(NH_2)$, $\delta(CH_3)$, $\delta(C–N)$, $\omega(=C–H)$, $\delta(NH_2)$ and $\delta_3(C–C)$ respectively[180,200–206]. From **Figure IV.2(b)**,

the characteristic absorption bands of TOPO could be assigned as follows: stretching vibrations of O–H modes at 3440 cm^{-1}, P=O and P–C stretching modes at 1146 and 1465 cm^{-1}, respectively [207–209]. In addition to the above absorption bands related to TOPO some faint bands could be observed between 1465 and 1145 cm^{-1} (marked by red color dotted box in **Figure IV.2(b)**); however, these bands were not observed at any other stage of processing after the addition of metal precursors. **Figure IV.2(c)** shows that the FTIR spectrum of the reaction mixture containing metal precursors, Cu(acac) and In(acac) along with OAm and TOPO at 50 °C. Due to the dissolution of metal precursors, change in absorption band positions and intensity were observed, which is highlighted in **Figure IV.2**. The characteristic bands at 3003, 2920, 2851, 1645, 1584, 1463, 1145, 966, 794 and 721 cm^{-1} from pure OAm and TOPO **(Figure IV.2(a) and (b))**, could still be observed in **Figure IV.2(c)**, indicating that amine and long-chain alkyl were still present. Relatively weak absorption bands at 1645, 1611 and 1584 cm^{-1}, which was present in pure OAm **(Figure IV.2(a))**, became more intense after the dissolution of metal precursors in OAm **(Figure IV.2(c))**, which indicated to the attachment of $–NH_2$ and –(CH) with the meal ions. The effect of the TOPO coordinating agent was also expected in the reaction mixture. The disappearance of P–C band at ~1465 cm^{-1}, and the shifting of P=O stretching mode at 1147 cm^{-1} **(Figure IV.2(b))** toward higher wavenumber 1161 cm−1 **(Figure IV.2(c))** suggested that the TOPO molecules were relatively weakly coordinating the metal ions via the P=O group. The absorption band at 1161 cm^{-1} remained unchanged on heating to 100 °C **(Figure IV.2(d))** and 150 °C **(Figure IV.2(e))**. A careful investigation shows **(Figure IV.2(f))** that the absorption band at 3297 cm^{-1}, which was assigned to $\nu s(NH_2)$ vibrational mode from pure OAm shifted towards the lower wavenumbers

of 3282, 3281 and 3277 cm^{-1} on heating to 50, 100 and 150 °C, respectively. This red shift was attributed to an increase in the coordination bonding of In^{3+}, Cu^{2+} with $–NH_2$. However, since the stability of the copper precursor is less as compare to the indium precursor, more number of coordination bonds between Cu^{2+} and $–NH_2$ is expected, when compare to In^{3+} and $–NH_2$ [47]. It is clear from the above observation that amines solvate the metal ions and can act as an effective surfactant to prevent aggregation. Hence, the OAm could play the principal role as a capping agent of the NPs, while TOPO acts as coordinating agent before addition of sulfur source.

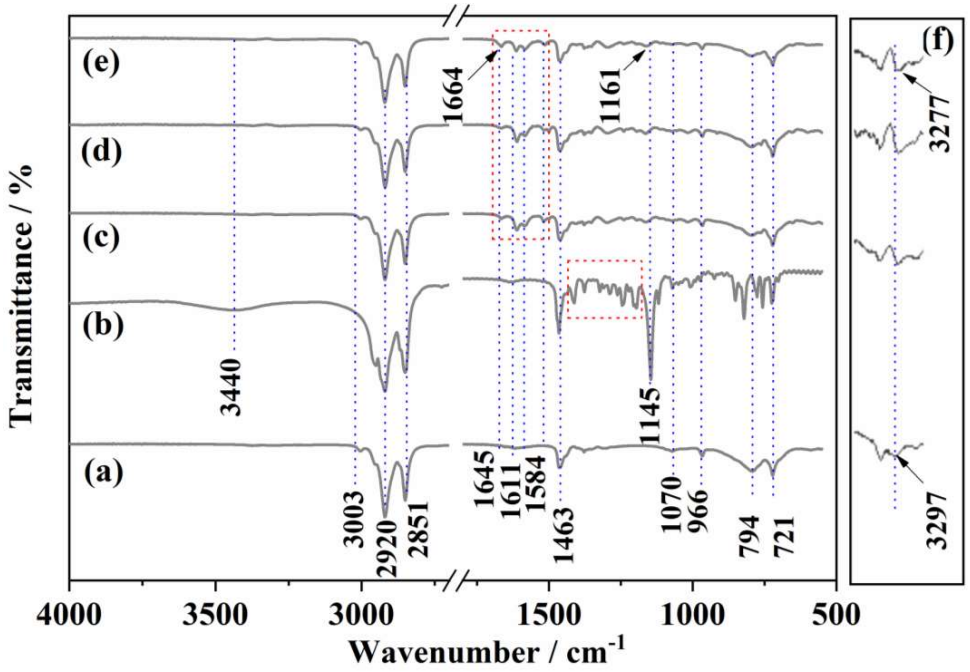

Figure IV.2 FTIR spectra of (a) OAm, (b) TOPO, reaction mixture that consist of Cu(acac)+In(acac)+TOPO + OAm at (c) 50 °C, (d) 100 °C, (e) 150 °C.

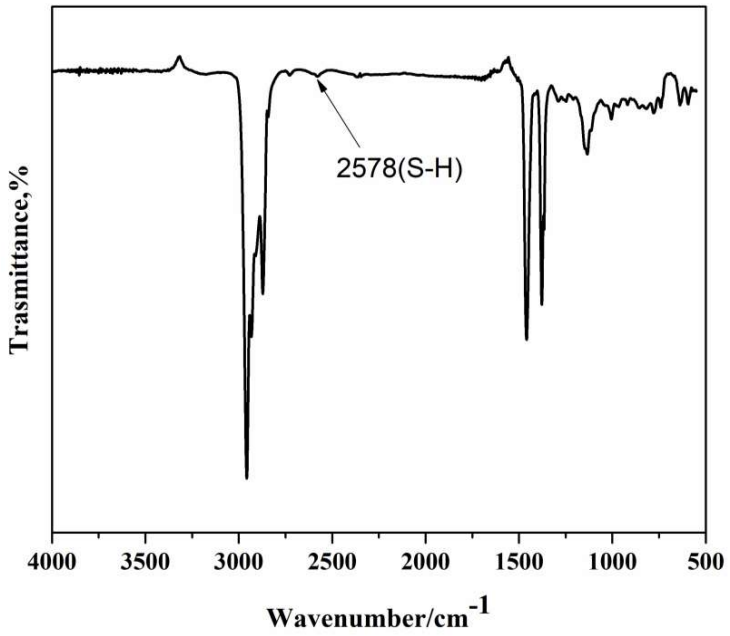

Figure IV.3 FT-IR spectra of pure tert- dodecanethiol, which was used as the sulfur source for synthesis of wz-CIS NPs.

The FTIR spectra of the samples extracted after the addition of sulfur source are shown in **Figure IV.4**. For reference, FTIR spectra of 1-DDT and t-DDT were also recorded as shown in **Figure IV.4(a) and (b)**, respectively, and the corresponding list of absorption bands are tabulated in **Table IV.2**. Pure 1-DDT had absorption bands at 2954, 2921, 2851, 1466, 1370, 721 and 650 cm^{-1}, which could be assigned to $\nu as(CH_3)$, $\nu as(\text{-}CH_2)$, $\nu s(\text{-}CH_2)$, $\delta as(CH_3)$, $\delta s(CH_3)$, δ(C–C) and δ(C–S), respectively [210–212]. In FTIR spectra of pure t-DDT, the absorption band had an identical position as compare to 1-DDT, albeit with more intense absorption bands at 2954, 1466 and 1376 cm^{-1}, which is demonstrative of the greater number (per unit volume) of $–CH_3$ functional group. **Figure IV.4(c)** shows that after adding thiols at 160 °C to the metal-precursor solution in OAm and TOPO, the absorption band shifted from 1161 cm^{-1} **(Figure IV.4(e))**, which was originally assigned to

P=O stretching mode, to 1152 cm^{-1} **(Figure IV.4(c))**. The absorption band of P=O stretching mode progressively shifted to 1150 **(Figure IV.4(d))**, 1128 **(Figure IV.4(e))** and 1118 cm^{-1} **(Figure IV.4(f) and (g))** on heating to 200, 250 and 290 °C, respectively. This progressive redshift in P=O was attributed to the fact that TOPO forms a comparatively strong bond with hexagonal Cu_2S and CIS NPs surface sites via its P=O group [207]. It was noticed from FTIR spectra of pure t-DDT **(Figure IV.3)** that a weak band at 2578 cm^{-1} corresponding to S–H vibration was present. However, this band was not present in the reaction mixture at 160 °C, which indicated the formation of metal–sulfide bonds [180, 213]. On further heating, the solution to 200 °C, absorption bands in the wavenumber range of 3003–2851 cm^{-1} and 1664-1256 cm^{-1} **(Figure IV.4(d))** had broadened. The broadening of these bands characterized the presence of a strong hydrogen bond. As the processing temperature was raised to 250 °C, the absorption bands at 1664 (corresponding to δ(-C=C)) and 1614 cm^{-1} (corresponding to NH_2 scissoring + N–H bending) at 200 °C had shifted to higher wavenumbers 1680 and 1622 cm^{-1} respectively, **(Figure IV.4(e))**. This band shifting reflects the reduction in the molecular mass of that OAm. On heating further to 290 and 310 °C, these bands did not shift further **(Figure IV.4(e) and (f))**. The absorption band at 652 cm^{-1} (attributed to the stretching vibration of C–S bond of 1-DDT depicted in **Figure IV.5**) shifted to lower wavenumber 620 cm^{-1} (**Figure IV.4(e), (f) and (g)**) indicating to the strong interaction of 1-DDT with the precipitated wz-CIS NPs at temperatures above 250 °C. It was also observed that absorption bands at 3003, 2954, 2921, 2851, 1581, 1466, 1376, 795 and 721 cm^{-1} disappeared on heating above 200 °C as shown in **Figure IV.4(e), (f) and (g)**. The absence of these bands in the spectra of wz-CIS NPs, revealed that the OAm was nearly removed by thiols

during the crystal growth [214]. These observations are in line with the reports of the removal of oleic acid (OA) and OAm surfactants on treatment with $(NH_4)_2S$ solution by the exchange of organic ligand with S^{2-} ions [200, 215]. The broad absorption band about 3405 cm^{-1} **(Figure IV.4(e-g))** was assigned to –OH stretching intermolecular hydrogen bonds due to the presence of small amount of moisture on the sample.

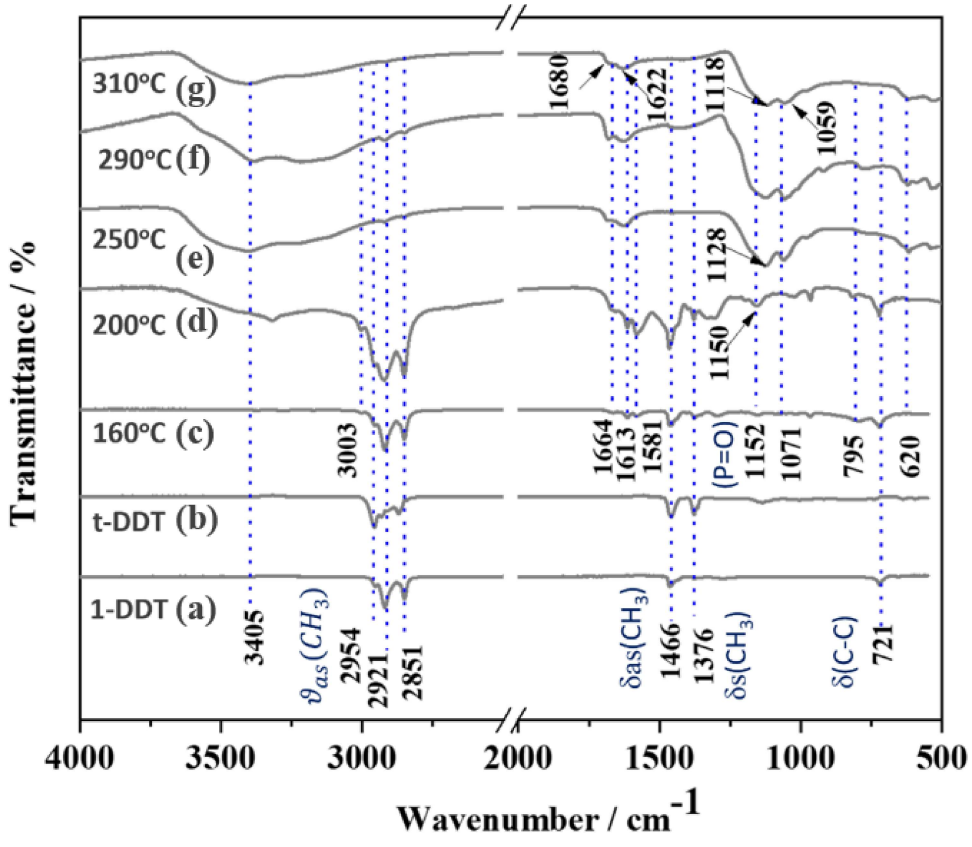

Figure IV.4 Infrared absorption spectra of pure form of (a)1-DDT, (b) t-DDT, and reaction mixture of Cu(acac) and In(acac) in TOOP and OAm with thoils at (c) 160 °C, (d) 200 °C, (e) 250 °C, (f) 290 °C, (g) 310 °C.

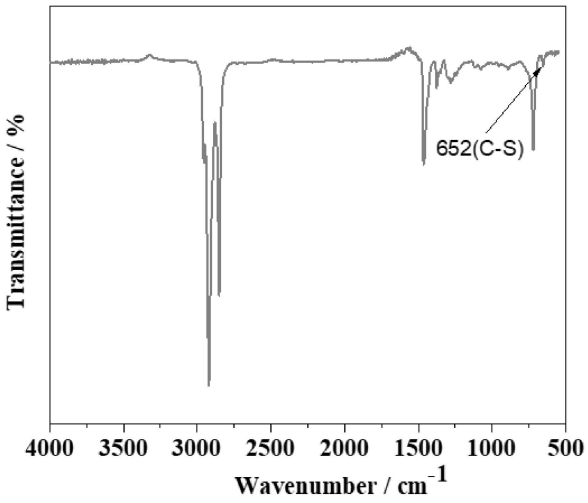

Figure IV.5 FT-IR spectra of pure 1- dodecanethiol, which was used as the sulfur source for synthesis of wz-CIS NPs.

Table IV.2 Infrared vibrational assignments for the intermediate and $CuInS_2$ NPs at different growth stages.

vibrational modes	frequency (cm−1)											
	OAm	TOPO	Temperature (°C)			1-DDT	t-DDT	Temperature (°C)				
			50	100	150			160	200	250	290	310
ν(OH)	---	3440	---	---	---	---	---	---	3403	3404	3394	3405
ν_s (NH_2)	3297	---	3282	3281	3277	---	---	3272	---	---	---	---
δ(=C-H)	3003		3003	3003	3003	---	---	3002	3004	---	---	---
δ(C-H)	2951	2951	2951	2951	2951	2953	2954	2954	2955	---	---	---
ν_{as}(C-H) and ν_s(C-H)	2920, 2851	2920, 2850	2920, 2851	2919, 2851	2920, 2851	2921, 2851	2932, 2871	2920, 2851	2922, 2852	2923, 2852	2920, 2851	---
δ(-C=C)	1652	---	1664	1664	1664	---	---	1664	1664	1680	---	---
δ(NH2)	1617	---	1611	1610	1613	---	---	1613	1614	1622	---	---
δ(NH2)	1593	---	1584	1583	1582	---	---	1581	1581	---	---	---
δas(CH3)	1463		1463	1461	1463	1466	1460	1463	1466	1463	---	---
ν(P-C)	---	1465	---	---	---	---	---	---	---	---	---	---
δs(CH3)	1377	1376	1377	1377	1376	1370	1377	1377	1378	---	---	---
ν(P=O)	---	1145	1162	1163	1161			1152	1150	1128	1128	1118
δ(C-N)	1070	1071	1071	1071	1071	---	---	---	---	---	---	---
	---	---	---	---	---	---	---	1052	1058	1060	1057	1057
trans ν(-C=)	966	---	966	966	966	---	965	966	965	---	---	---
δ(NH2)	791	---	794	794	794	---	---	794	789	---	---	---
δ(C-C)	721	---	721	722	722	720	---	722	722	---	---	---
δ(C-S)	---	---	---	---	---	650	---	650	650	620	620	620

IV.4.3 TEM Analysis

The correlation between structure and composition with the morphology of the as-synthesized wurtzite NPs has been studied in TEM. The bright-field images of the sample extracted at 160 ℃ and 200 ℃ are shown in **Figure IV.6(a) and (e)**, respectively. It could be observed from the images that a considerable amount of amorphous phase in which tiny particles were present in the sample extracted at 160 and 200 ℃, while the nanoparticles were embedded within the amorphous content. It can be observed from the bright field images **(Figure IV.6(a) and (e))** that a large number of nanoparticles were nearly oval-shaped. The average length and width of the nanoparticles were 42 ± 5.5 nm and 27 ± 3.1 nm at 160 ℃. The SAED pattern **(Figure IV.6(b))** obtained at 160 ℃ after addition of thiols, showed three diffraction rings corresponding to their planes of hexagonal Cu_2S phase, which was in good agreement with the observations made from the X-ray pattern **(Figure IV.1)**. At this stage, ligand exchange began as observed from the FTIR study **(Figure IV.4)**. The pre-formation of Cu–S compound has been proposed earlier by several investigators [44, 190, 193,196, 215]. Interestingly, faint diffraction rings, which could be indexed to planes of In_2S_3 could also be observed for the sample extracted at 160 ℃. These Debye rings were not detected by XRD. Detailed analysis of the diffraction pattern is listed in **Table IV.3**. This clearly indicates that the formation of In_2S_3 compound cannot be ruled out. However, these compounds were not significant in volume and could only be detected by the highly selective sampling in TEM. While on the other hand, the Cu_2S phase is much more dominant, which has been predicted by other investigators also [190, 193, 216]. The preferential formation rate of copper sulfide was mainly attributed to two factors:

i) stronger Cu^{+}-thiol ion interaction than In^{3+}-thiol as predicted by the hard and soft acid and base (HSAB) theory, and ii) preferential binding of active ligands (OAm and TOPO) with In^{3+} ions preventing the formation of In–S bonds, which makes Cu^{+} more active than In^{3+} ions in the solution.

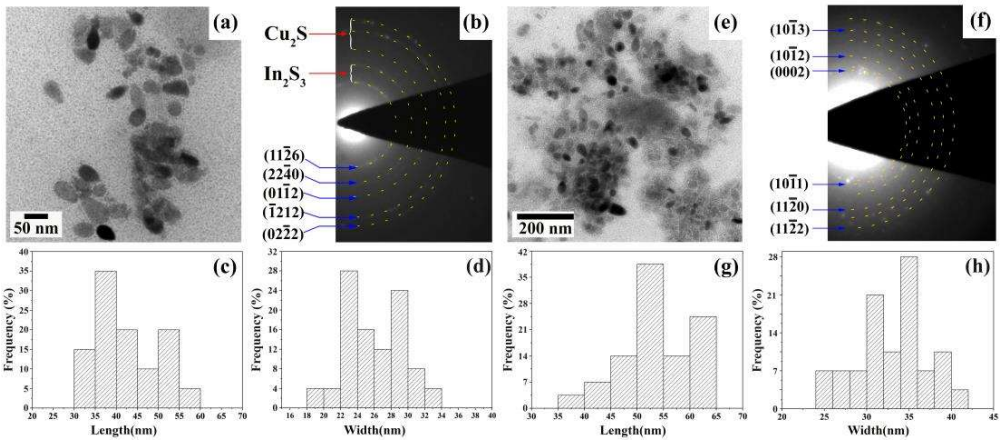

Figure IV.6 (a) Bright field TEM micrographs demonstrating the evolution of size distribution, (b) corresponding SAED pattern, (c) length and (d) width distribution histogram of oval-shaped nanoparticles at 160 °C, and (e) Bright field TEM image, (f) SAED pattern, (g) length and and (h) width distribution histogram of oval-shaped nanoparticle at 200 °C.

Histograms have been drawn by measuring more than 100 particles to evaluate the size distribution at different stages of processing. For the samples extracted at 160 °C, the morphology of the NPs is mostly oval-shaped with 30–60 nm in length **(Figure IV.6(c))** and 18–31 nm in width **(Figure IV.6(d))**. SAED of the sample collected at 200 °C showed diffraction rings corresponding to $(10\bar{1}3)$, $(10\bar{1}2)$, (0002), $(10\bar{1}1)$, $(11\bar{2}0)$ and $(11\bar{2}2)$ crystallographic planes of Cu_2S phase **(Figure IV.6(f))**, which match with the X-ray pattern as shown in **Figure IV.1(b)**. At this

stage, the NPs were mostly oval with 42–60 nm in length and 24–42 nm in width, while the average length and width was 49 ± 5.3 and 32 ± 3.8 nm, respectively **(Figure IV.6(g) and (h))**.

On heating further to 250 °C, Bright field TEM images showed uniform oval-shaped particles with narrow ends and quasi-round central body having a mean width and length of 53 ± 4.8 nm and 33 ± 2.6 nm, respectively **(Figure IV.7(a))**. The tiny amorphous particles in the background are reduced in number, indicating their dissolution or joining with the larger crystalline particles. The particle size observed in TEM was close to the crystallite size (~45 nm) estimated from XRD peak broadening, which indicated that the particles were single crystals. The lattice constants, calculated using the Nelson-Riley function, was estimated as a = 3.90 ± 0.01 Å and c = 6.49 ± 0.08 Å. The SAED pattern (inert in **Figure IV.7(a)**) showed seven characteristic diffraction rings, which could be indexed to $(10\bar{1}0)$, (0002), $(10\bar{1}1)$, $(10\bar{1}2)$, $(11\bar{2}0)$, $(10\bar{1}3)$ and $(11\bar{2}2)$ crystallographic plane of wz-CIS [172, 182]. Detailed analysis of the diffraction pattern of wz-CIS is shown in **Table IV.3**. From the FTIR and XRD analysis, it was confirmed that the wz-CIS formed at around 250 °C during processing. FFT collected from the HRTEM images provide information about the periodicity of the atomic structure, which may be associated to the electron diffraction patterns recorded at the back focal plane of the objective lens [217]. The FFT and the HRTEM image **(Figure IV.7(b))** showed lattice fringes having d-spacing close to 0.3 nm and 0.33 nm, which matched with the spacing of (0002) and $(10\bar{1}0)$ planes of CIS, respectively.

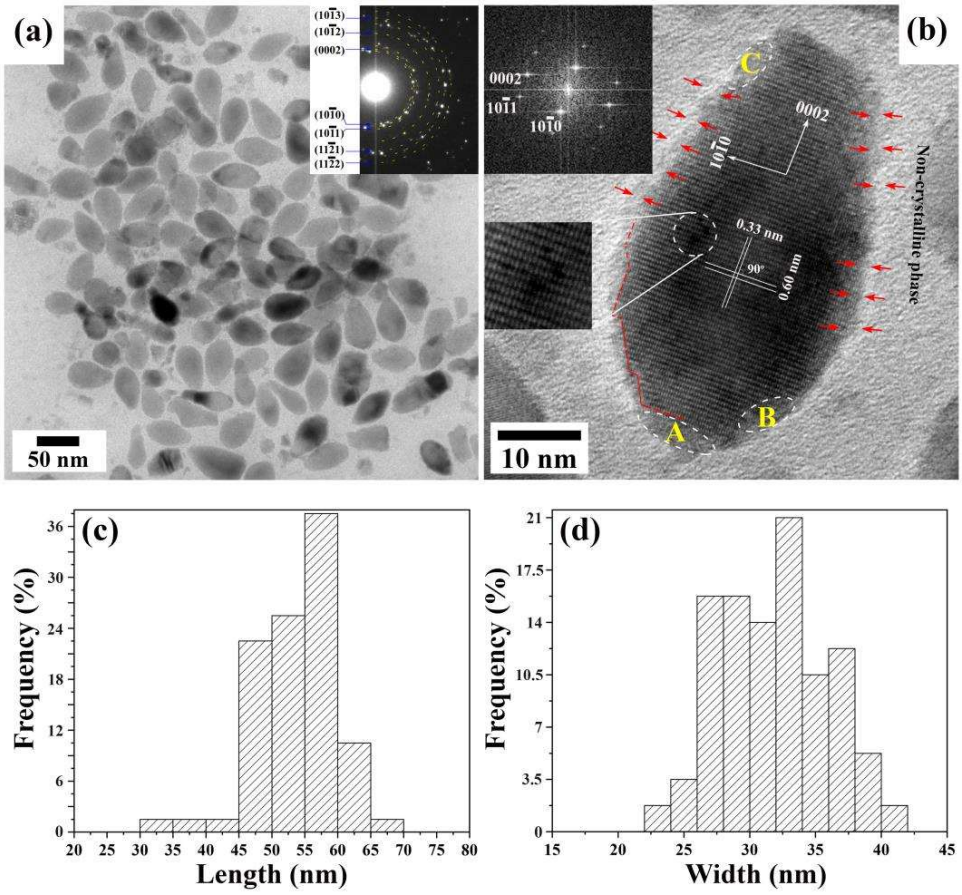

Figure IV.7 (a) Bright field TEM image with inserted SAED pattern, (b) HRTEM image of a CIS NP showing facets and preferential growth along c-direction and (inset) Fast Fourier transform (FFT) pattern. Misfit dislocation are marked with a dotted circle (right bottom of **Figure IV.7**(b), red arrows represent the amorphous layers on the surface, (c) length and (d) width distribution histogram of oval-shaped nanoparticle at 250 °C.

Further investigation of HRTEM revealed the presence of misfit dislocation, one such dislocation is marked as the white dotted circle; an enlarged image of fringe is shown as an inset in **Figure IV.7(b)**. Misfit dislocation might have formed due to the diffusion of indium in the copper sulfide structure. Faint contrast was shown in

Figure IV.7(b) (marked by a white dotted ellipse (A, B and C)) and the red arrows show the amorphous layer. The amorphous layer was attributed to the presence of OAm on the surface of the wz-CIS NPs. Size distribution was evaluated by counting more than 200 particles and is shown in **Figure IV.7(c)**. The NPs were oval-shaped with 30–70 nm in length and 24–40 nm in width **(Figure IV.7(d))**, while the number of tiny amorphous particles further reduced **(Figure IV.7(a))**.

As the temperature was raised to 290 °C, the uniformly distributed oval-shaped NPs grew in size to the mean length and width of 59 ± 5.3 nm and 32 ± 3.7 nm, respectively as can be observed from the bright field TEM image in **Figure IV.8(a)**, while the tiny particles in the background became scarce. The particle size measured from TEM was again close to the volume averaged crystallite size of ~47 nm as obtained from XRD data. The lattice constants calculated using the Nelson-Riley function were estimated as a = 3.91 ± 0.02 Å and c = 6.48 ± 0.06 Å. In the SAED pattern of the NPs synthesized at 290 °C, each ring was accounted for wz-CIS and was indexed to (0002), $(10\bar{1}1)$, $(10\bar{1}2)$, $(10\bar{1}3)$, $(20\bar{2}0)$ and $(20\bar{2}3)$ crystallographic planes (inset in **Figure IV.8(a)**).

The facets preferentially grow along the (0002) plane with an interplanar spacing of 0.30 nm. Lattice fringes corresponding to $(10\bar{1}1)$ plane having a d-spacing close to 0.28 nm could be deciphered from the FFT of the HRTEM image. Lesser number of defects were observed **(Figure IV.8(b)**, marked at white circle) in the sample synthesized at 290 °C, as compared to the sample extracted at 250 °C. This could be related to the structural relaxation during high temperature synthesis and enhanced diffusion of In^{3+} ions into the lattice. The morphology of the particles was oval with 42–62 nm in length and 24–40 nm in width **(Figure IV.8(g) and (h))**.

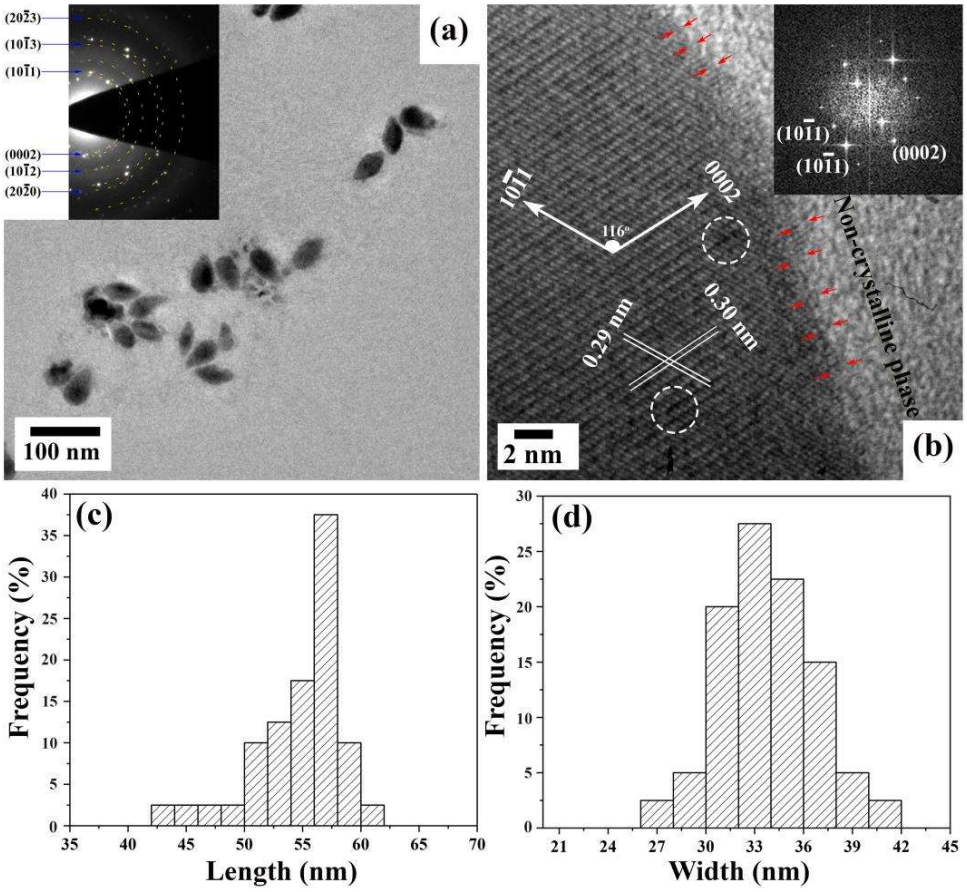

Figure IV.8 (a) Bright field TEM image with SAED pattern (inset), (b) HRTEM image of a CIS NP shows that the facets preferentially grow along c-direction. FFT of the image is shown in the inset. Misfit dislocations are marked with white dotted circles and red arrows represent the amorphous layers on the surface. (c) Length and (d) Width distribution histogram of oval-shaped nanoparticle after synthesis at 290 °C.

The sample was finally heated to 310 °C, was held at that temperature for 60 min and subsequently cooled down to RT. The bright field TEM images showed that the NPs still had uniform oval morphology with increased mean width and length of 60 ± 5.1 nm and 33 ± 3.7 nm, respectively, which again was in good agreement

with the crystallite size ~50 nm as calculated from the powder X-ray diffraction patterns **(Figure IV.1(a))** using Scherrer equation. A representative BF image is depicted in **Figure IV.9(a)**. The lattice constants as calculated using the Nelson-Riley function was estimated to be a = 3.92 ± 0.03 Å and c = 6.43 ± 0.04 Å. The SAED pattern could be indexed to (0002), (01$\bar{1}$1), (01$\bar{1}$2), (01$\bar{1}$3) and (0004) crystallographic planes of pure wz-CIS (inset in **Figure IV.9(a)**).

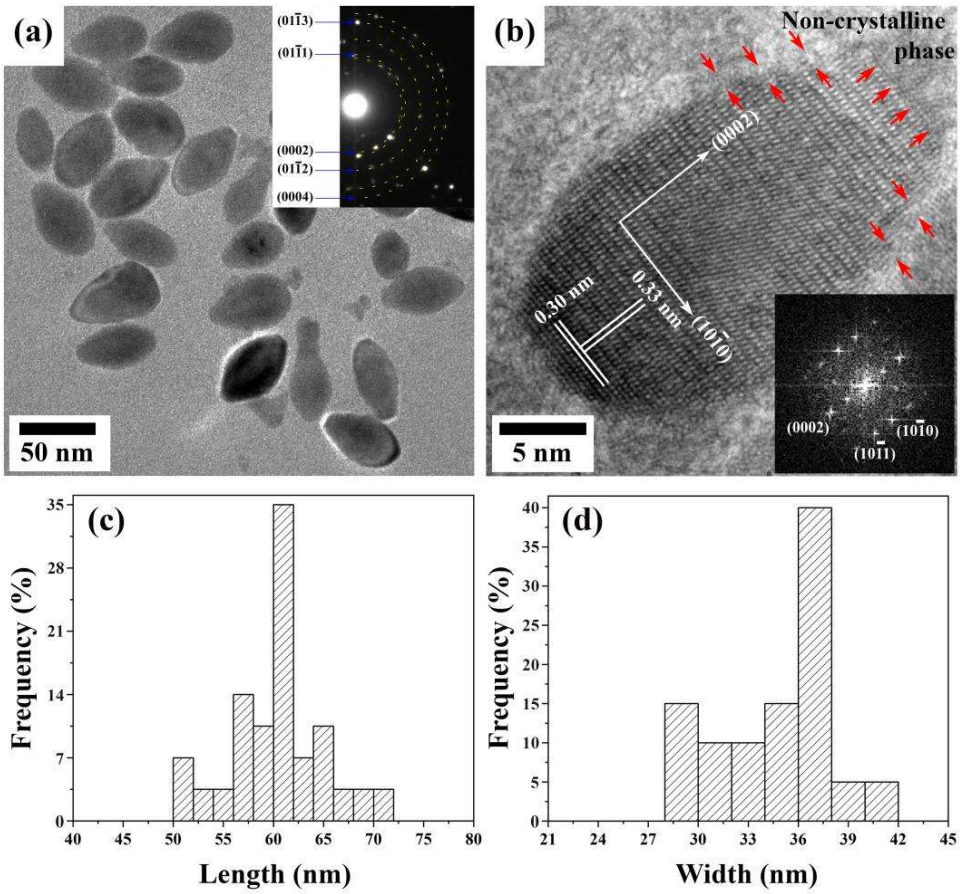

Figure IV.9 (a) Bright field TEM image with SAED pattern (inset), (b) HRTEM image of CIS NPs show mildly faceted growth and preferential growth along c-direction. Fast Fourier transform (FFT) of the image is given in the inset. Red

arrows indicate the amorphous layers on the surface. (c) length and (d) width distribution histogram of the oval-shaped nanoparticle after processing at 310 °C.

HRTEM images in **Figure IV.9(b)** showed that the length direction of the oval-shaped nanoparticle coincided with [0002], which indicated that the [0002] was the preferential growth direction. The growth behavior of the nanoparticles extracted at all temperatures indicated that [0002] was the favored growth direction and the growth kinetics plateaued after 200 °C. Faster growth along the c-direction may be attributed to the ease of attachment of incoming ionic species on the c-plane and in turn, rather slow kinetics of diffusional attachment of ionic species on other planar facets. The misfits and defects, which were observed in the samples extracted at 290 °C, were largely absent for the sample extracted after 60 min holding at 310 °C. This could be attributed to the annealing and complete diffusion of In^{+3} ion in unit cell. The morphology of the particles remained oval with 50–71 nm in length and 26–40 nm in width **(Figure IV.9(c) and (d))**.

Table IV.3 Detailed analysis of diffraction pattern of wurtzite $CuInS_2$ and Cu_2S, and In_2S.

			Observed	Reported	
Crystal structure	**Growth temperature**	**Miller indices**	**d-spacing(Å)**	**d-spacing(Å)**	**Reference code**
In_2S_3	160ºC	$(11\bar{2}6)$	3.83	3.81	40-008-13
		$(22\bar{4}0)$	2.67	2.69	
wz-Cu_2S	160ºC	$(01\bar{1}2)$	2.46	2.41	98-004-5258
		$(02\bar{2}1)$	1.70	1.70	
		$(02\bar{2}2)$	1.55	1.53	
	200ºC	$(10\bar{1}3)$	1.83	1.85	98-001-1585
		$(10\bar{1}2)$	2.39	2.37	
		(0002)	3.28	3.33	
		$(10\bar{1}1)$	2.88	3.00	
		$(11\bar{2}0)$	1.98	1.94	
		$(11\bar{2}2)$	1.67	1.68	
wz-CIS	250ºC	$(10\bar{1}0)$	3.32	3.38	98-011-6428
		(0002)	3.13	3.21	
		$(10\bar{1}1)$	2.88	2.99	
		$(10\bar{1}2)$	2.25	2.33	
		$(11\bar{2}0)$	1.89	1.95	
		$(10\bar{1}3)$	1.76	1.81	
		$(11\bar{2}2)$	1.60	1.67	
	290ºC	(0002)	3.26	3.21	98-011-6428
		$(10\bar{1}1)$	3.05	2.99	
		$(10\bar{1}2)$	2.37	2.33	
		$(10\bar{1}3)$	1.84	1.81	
		$(20\bar{2}0)$	1.71	1.69	
		$(20\bar{2}3)$	1.37	1.32	
	310ºC	(0002)	3.10	3.21	98-011-6428
		$(10\bar{1}1)$	2.81	2.99	
		$(10\bar{1}2)$	2.25	2.33	
		$(10\bar{1}3)$	1.74	1.81	
		(0004)	1.59	1.61	

The change in nanoparticle size as a function of temperature is plotted in **Figure IV.10(a)**. At 160℃, after the addition of sulfur source, the nanoparticles were primarily Cu_2S phase having a width ~27 nm and length ~42 nm. On increasing the temperature to 200 ℃, particles grew by 22% in width and only 14% in length. The nanoparticles grew more in width than length direction. It has been observed from XRD and electron microscopy that the formation of CIS initiates at 250 ℃ by diffusion of In^{3+} from the solution, while at the same time, NPs continues to grow in size. Between 200 and 310 ℃, particles grew in the length direction by about 25% while only 6.25% in width direction **(Figure IV.10(a))**. NPs were primarily Cu_2S, here it could possible that the growth rate in $[10\bar{1}0]$ direction was greater than [0002] direction, while above 250 ℃ significant In^{3+} incorporations happened and growth direction in [0002] was greater than $[10\bar{1}0]$ direction, during later stages of processing, relatively less growth happened without altering the chemistry significantly, as observed in **Figure IV.8(a)** and **Figure IV.9(a)**. One reason for the growth direction switching could be the change in atomic density and electrostatic interaction due to the incorporation of In^{3+}. **Figure IV.10(b)** shows the variation of Cu/In ration at different temperatures. Analysis of six randomly selected areas gave average Cu/In ratios of 9.0, 3.7, 2.90 and 2.0 for 160, 200, 250 and 290 ℃ respectively. This flexibility in stoichiometry is allowed as copper and indium share the lattice sites. At the beginning of the reaction at 160 ℃, the copper content was very high (Cu/In = 9.0). The elemental composition ratio Cu:In:S of sample collected after the complete process was 1.0:0.47:1.6, which is compositionally different from the expected 1:1:2 stoichiometry for $CuInS_2$. Still, $Cu_{1.0}In_{0.47}S_{1.6}$ composition falls within the phase space for wz-Cu-In-S [89]. **Figure IV.10(c)** depicts the variation of crystallite size as a function of temperature, which reflects

a nearly linear increase in the crystallite size from ~18 nm to ~45 nm as the reaction mixture was heated from 160 to 250°C respectively. However, it was noticed that after 250 °C the increase in crystallite size was marginal.

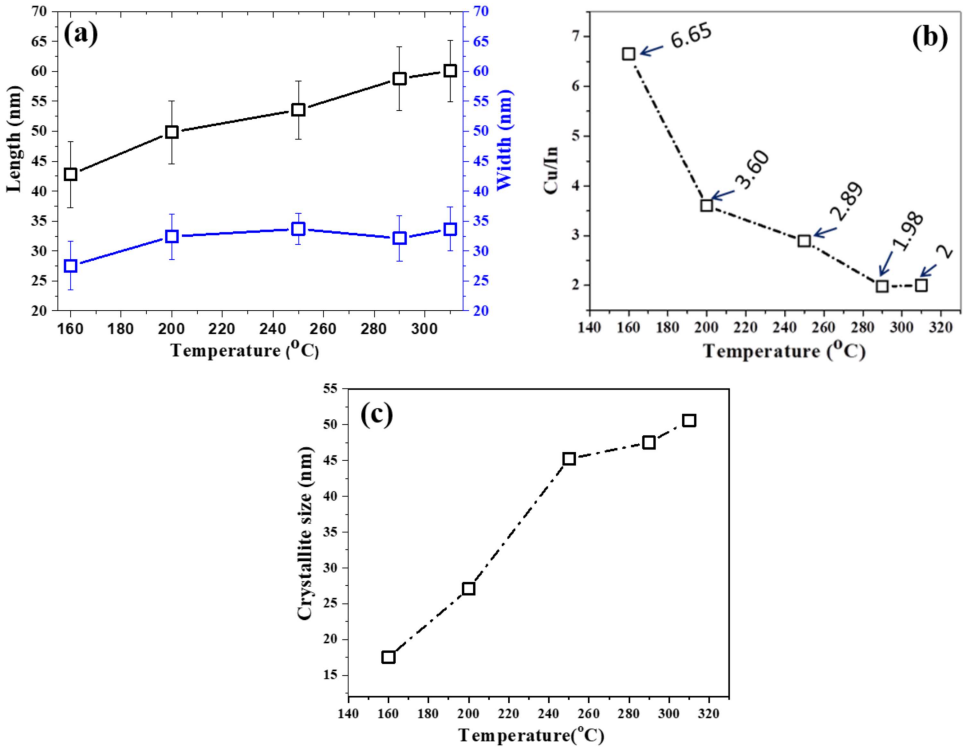

Figure IV.10 (a) The detailed evolution of the length and width of the nanoparticles, (b) Variation of Cu/In ratio, and (c) change of crystallite size as a function of growth temperature of reaction mixture.

To confirm the spatial distribution of individual elements (Cu, In and S), chemical analysis was performed in scanning transmission electron microscopy (STEM) mode for the sample synthesized at 310°C. Bright field TEM image of one of the particle clusters chosen for STEM is depicted in **Figure IV.11(a)**. A high-angle annular dark-field (HAADF) image of a nanoparticles cluster **(Figure IV.11(b))** were featureless and was uniformly bright throughout, indicating a uniform

chemical composition. STEM-EDS elemental mapping of the randomly selected region (marked by square box) **(Figure IV.11(d–f))** illustrates that all the elements Cu, In, and S were homogeneously distributed.

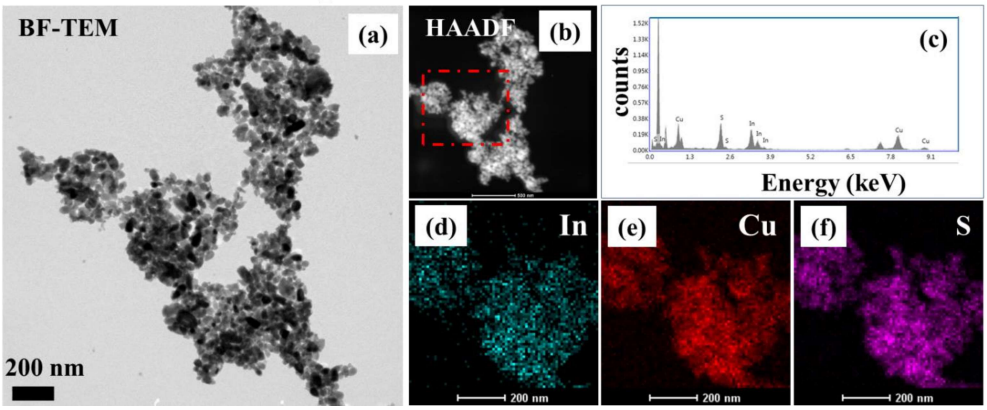

Figure IV.11 (a) Bright field TEM image, (b) high-angle annular dark field image, (c) EDS spectra, and (d–f) STEM-EDS mapping of individual element of wz-CIS NPs for sample collected at 310 °C.

IV.5 Discussion

In the present work, wz-CIS has been synthesized by wet chemistry route and its formation mechanism has been explored. It has been demonstrated from the XRD, FTIR and TEM results that Cu_2S nanoparticles nucleate after the addition of sulfur source at around 160–200 °C, which on further processing to higher temperatures (>250 °C) leads to the formation of the metastable wz-CIS phase. Here, M(acac), [M = Cu^{2+}, In^{3+}] are co-ordination complexes resulting from the acetlyacetonate anion. As per FTIR results, active ligand OAm forms complex compounds with the metal ions of the M(acac) precursor at 50–150 °C **(Figure IV.2(c–e))**, leading to

metastable compounds that can act as secondary precursors (M(acac)-. nNH_2), it decomposes with the addition of sulfur(thiols) source at 160 °C and forms copper sulfide phase, which on further processing results in the formation of wz-CIS NPs. Based on Covalent Bond Classification (CBC), TOPO and OAm are L-type ligands, both ligands act as Lewis bases that bond to Lewis acidic sites i.e., Cu^{2+}, In^{3+} by a dipolar bond that donate two electrons to the nanocrystal surface. It has been clearly demonstrated that OAm and TOPO successfully bond the metal ions (schematically depicted in **Figure IV.12**). However, the effect of OAm is stronger than the TOPO, this may be because of the fact that OAm has a stronger Lewis base and prefers to combine more strongly with Lewis's acid (i.e Cu and In metal ions). On the other hand, according to the hard and soft acid and base (HSAB) theory, the In^{3+} is harder acid than Cu^{2+}, and comparatively weakly polarizable [218]. Therefore, In^{3+} had a greater tendency to form coordination compound with OAm as compared to Cu^{2+}.

On dodecanthiol addition at 160 °C, copper sulfide formed, which was not well crystallized as was observed from the X-ray pattern **(Figure IV.1(a) and (b))** and the TEM results **(Figure IV.6(b) and (f))**. SAED pattern confirmed the nucleation of Cu_2S as a major phase **(Figure IV.6(a) and (b))**. Some In_2S_3 was also picked up by the TEM diffraction pattern, which was largely absent in the XRD pattern. This indicated that some trace amount of In_2S_3 was also present at this temperature. A similar observation was earlier made by Kuzuya *et al.* [191], which was attributed to the stability of the In-OAm complex. The reducing property of the dodecanthiol resulted in an increased concentration of Cu^+ ions in the reaction mixture. The Cu^{2+} was reduced to Cu^+ by thiols due to its low reduction potential of +0.159 V versus Normal Hydrogen Electrode [219]. This was appropriate for the formation of

copper sulfide nanoparticles. XRD **(Figure IV.1)** and TEM **(Figure IV.6(f))** results revealed the presence of Cu_2S up to 200 °C with no sign of indium incorporation at this growth stage regardless of its presence in solution. On heating to a higher temperature to 250 °C, the various molecular bonds associated with TOPO and OAm begin to disappear which leads to ligand exchange **(Figure IV.4(c))**. As growth temperature is increased to 250 °C **(Figure IV.1 and IV.7)**, the chalcocite Cu_2S phase is in the superionic conducting state [220] and at the same time Cu(I) in Cu_2S exhibits high mobility [221]. Interstitial sites formed by the sulfur sublattice are randomly occupied by the Cu^+ ions. Due to the high mobility of Cu^+ ions, there was cation exchange with In^{3+} ion and led to the formation and growth of wz-CIS NPs [176]. As a smaller (Cu^+) ion is replaced by the bigger one (In^{3+}), it results in the increase of lattice constants, as shown in **Figure IV.1**. This cation exchange is facilitated by comparable ionic radii of Cu(I) (0.77 Å) and In(III) (0.80 Å) as was suggested in earlier reports, where wz-CIS NPs was shown to form by the incorporation of In^{3+} into the Cu–S crystal nuclei through the diffusion and/or cation exchange [176, 182, 222]. It was understood that the nucleation and growth of particles were very fast after the addition of sulfur source, as a result, some particles could even grow as large as 50 nm, a similar observation also made by Norako et al. [193]. However, the formation of CuS, Cu_2S and In_2S_3 phases was missing as the growth process was very fast as per the reports.

There were some very small particles also visible, which reduced in number as the temperature was raised as can be seen from in the background of the TEM bright-field images shown in **Figure IV.6(a)-Figure IV.9(a)**. The number of tiny particles reduced as the processing temperature was raised without any significant growth. This indicates that the smaller particle kept dissolving and reduced in number while

the larger particles grew at the cost of these smaller particles, a mechanism widely known as Ostwald ripening. A similar observation was made earlier by Norako et al. [193] in the solution processing of wz-CIS. **Figure IV.12** shows a schematic representation summarizing the growth stage along with corresponding nanoparticle growth orientation. The growth kinetic was very fast in between 160 °C and 200 °C, and it was sluggish above the 200 °C, as can be observed from **Figure IV.10(a)**.

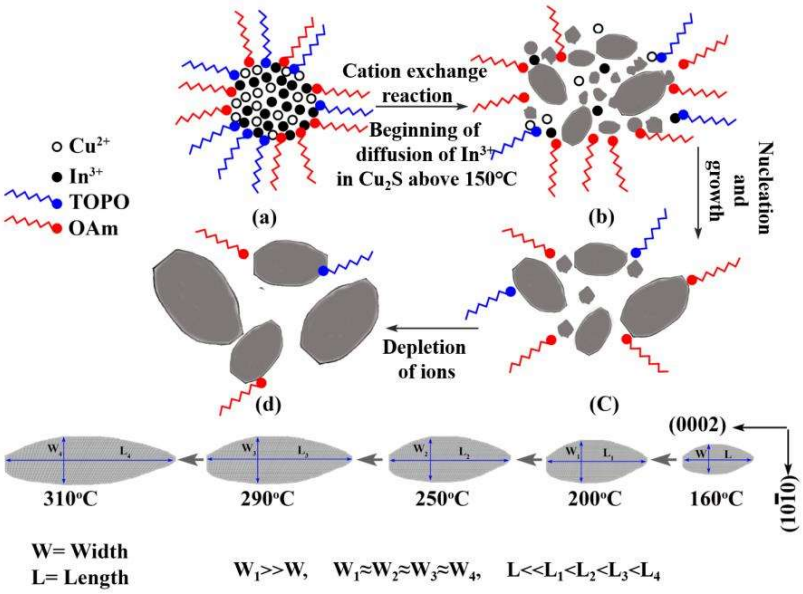

Figure IV.12 Schematic represent the formation of wz-CIS NPs, which shows the formation of copper sulfide at earlier stage with dissociation of metal complexes and addition of sulfur source. As growth temperature increase cation exchange reaction favour the formation of wz-CIS with [0002] as preferred growth direction.

However, it was noticed that growth in width direction that falls in range 18–34 nm for 160 °C **(Figure IV.6(d))**, thereafter (T ≥ 200 °C) it always remained close to the range of 24–41 nm for further growth stages **(Figure IV.10(a))**. The preferential

attachment of indium/copper ion was on (0002) facet than the $(10\bar{1}0)$ facet that causes the NP to elongate along the length. In 0002 projection of wz-CIS structure, it has layer structure as Cu^{+}/In^{3+} layer then S^{2-} layer again Cu^{+}/In^{3+} layer and so on, now (0002) planes are charge plane since they have four dangling bonds (unsatisfied valence) of sulfur, so the chance of the easy attachment of Cu–S complex is more due to higher reactivity and higher surface energy. On the other hand, $(10\bar{1}0)$ plane has a less charge plane as it has two sulfur and two metal ions, which favored the ion exchange reaction [223]. So, preferential elongated nanoparticles were generated, as depicted in **Figure IV.12(bottom)**.

IV.6 Concluding Remarks

$CuInS_2$ was synthesized by the hot injection technique in a Schlenk line. The detailed nanoparticle formation and growth mechanism were studied using XRD, FTIR and TEM. XRD patterns of the nanoparticle show a gradual sharpening of the reflections as temperature increased, representing NPs growth. Cu_2S phase was observed to form between 160 and 200 ℃ after the injection of thiols, which converted to the wz-Cu-In-S phase through the incorporation of In^{+3} ions on subsequent processing. The HRTEM and FFT pattern indicates that the wz-CIS oval shape NPs grow along [0002] direction and is enclosed by $(10\bar{1}1)$ and $(10\bar{1}0)$ crystallographic facets. The FTIR indicated that the ligand strength between the monomers and TOPO is weaker than that between the monomer and OLA. In^{3+} had a greater tendency to form coordination compound with OAm as compared to Cu^{+2}, which favored the preformation of Cu_2S before In incorporation by ion exchange at higher temperatures (>250 ℃), leading to the formation of $CuInS_2$.